Schweizerischer Erdbebendienst
Service Sismologique Suisse
Servizio Sismico Svizzero
Swiss Seismological Service

ETH zürich

# SITE CHARACTERIZATION REPORT

# SWIS: Winterthur (ZH) - Kantonsspital

Manuel Hobiger, Clotaire Michel, Jan Burjánek, Donat Fäh


Last Modification: 24th February, 2017

Schweizerischer Erdbebendienst (SED)
Service Sismologique Suisse
Servizio Sismico Svizzero
Servizi da Terratrembels Svizzer

ETH Zürich
Sonneggstrasse 5
8092 Zürich
Schweiz
manuel.hobiger@sed.ethz.ch

# Contents

# 1 Summary

The modern free-field SSMNet station SWIS was built in Winterthur at the site of the Kantonsspital. We performed passive seismic array measurements with two configurations for the site characterization. The measurements showed that the fundamental frequency of the structure beneath the station is at about 2.5 Hz.
The array measurements were analyzed with three different techniques, namely 3-component HRFK, WaveDec and SPAC. All techniques gave coincident dispersion curves. The dispersion curves of the fundamental modes of Love and Rayleigh waves could be retrieved at both arrays. Joint inversions of dispersion and ellipticity curves yielded principally an underground profile made up of unconsolidated and consolidated sediments in the uppermost 40 m, where a marl layer starts. The $V_{S30}$ value is around 480 m/s, corresponding to soil class B (EC8) or C (SIA261).

# 2 Introduction

In the framework of the second phase of the Swiss Strong Motion Network (SSMNet) renewal project, a new station was planned in the city of Winterthur. The site selection process resulted in the Kantonsspital as the best location. The new station, called SWIS, was constructed on the eastern part of the hospital and went operational on 27 February 2015. The location of the station is shown in Fig. 1.

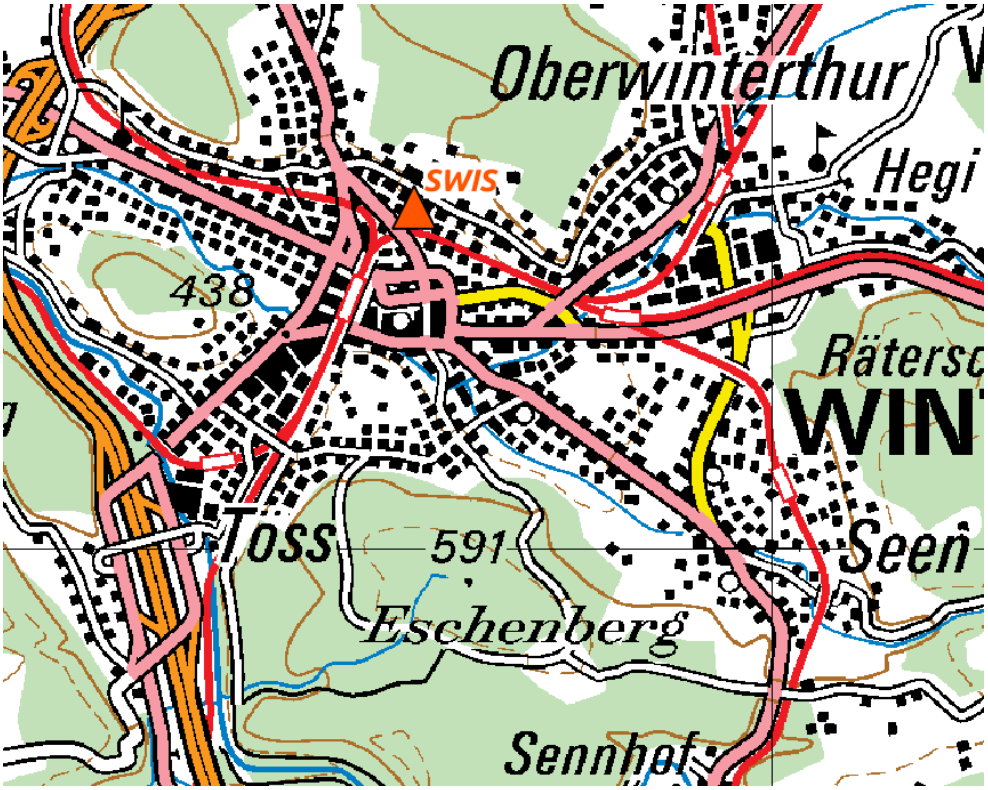


Figure 1: Map showing the location of station SWIS next to the Kantonsspital in Winterthur.

# 3 Geological setting

A geological map of the surroundings of station SWIS is shown in Fig. 2. A borehole on the hospital area indicates a marl layer at a depth of 36 m, certainly overlain by quaternary sediments.

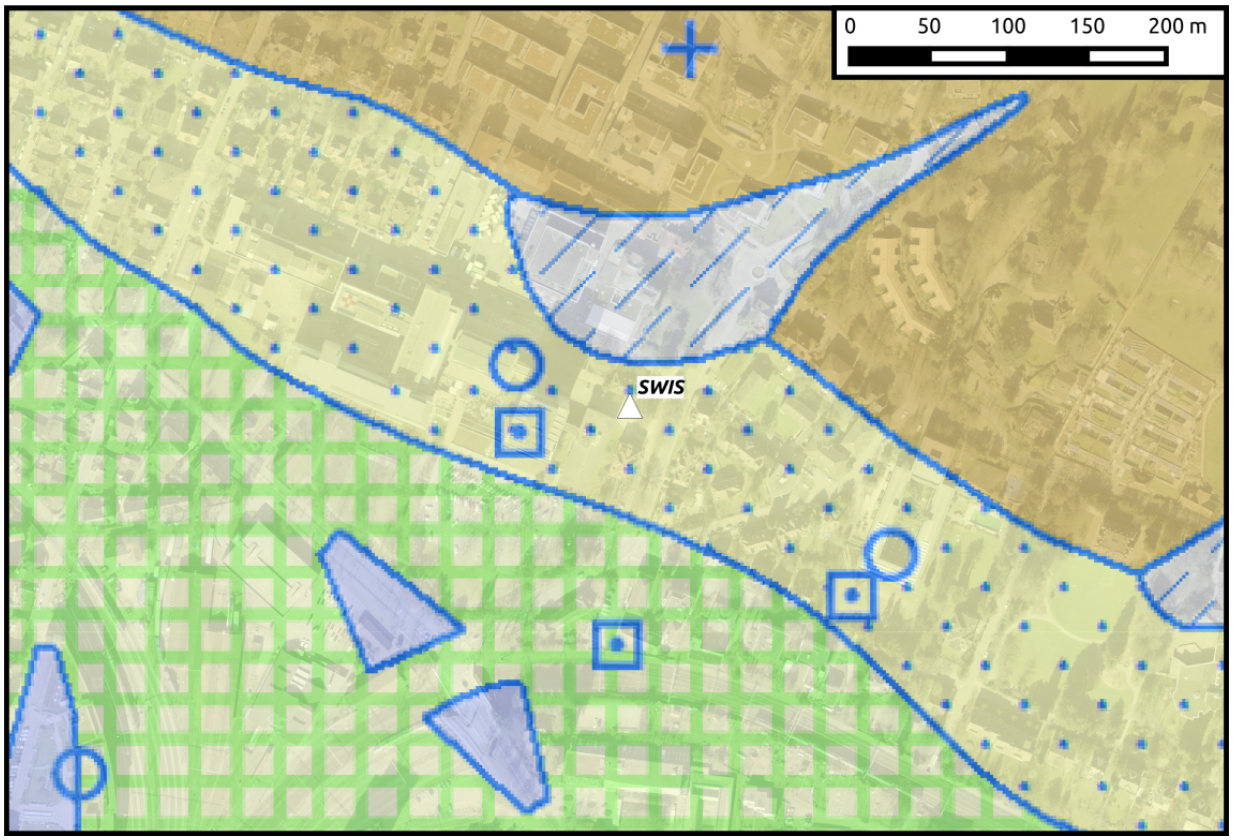


Figure 2: Geological map of the area around station SWIS. According to the geological atlas, station SWIS lies on silt (yellow area with blue dots). The gray area with blue dashes corresponds to an alluvial cone, the brown area to marl and the green-checkered area to glacial rubbles.

# 4 Site characterization

## 4.1 Measurements and data set

In order to characterize the local underground structure around station SWIS, passive seismic array measurements were carried out on 2015 April 25. The layout of the two seismic arrays is shown in Fig. 3. As the available space for an array measurement is limited by the hospital building, we deployed a smaller array close to the seismic station and a larger one extending to the parking space on the southern side.
Array 1 was installed first, it consisted of 12 stations in total. It was planned as consisting of a central station and two rings of three and five stations, respectively, with radii of 8 and 24 m. Three additional stations were installed in the west and south, to increase the accessible wavelengths. The station names of this array are composed of "SWIS" followed by a two-digit number between 2 and 14 (there is no station SWIS08).
In order to measure longer wavelengths and reach deeper layers, a second array was built by moving six of the stations to other locations and installing an additional station. The layout of the second array is less systematic and covers mainly the big parking space in the south of the hospital. The stations in the second array have station names consisting of "SWIS" followed by two-digit numbers between 21 and 33.
The parameters of both arrays are given in Table 1.
The station locations have been measured by a differential GPS system (Leica Viva GS10) which was set up to measure with a precision better than 5 cm. All station locations were measured with better precisions than this except for station SWIS27 in the large array. This station was located below a large building and the GPS measurement only had a precision of 1.05 m.

Table 1: List of the seismic array measurements in Winterthur.

| Array name | Number of sensors | Minimum interstation distance [m] | Maximum interstation distance [m] | Recording time [s] |
|---|---|---|---|---|
| 1 | 12 | 8.0 | 92.4 | 5640 |
| 2 | 13 | 23.9 | 207.1 | 7140 |

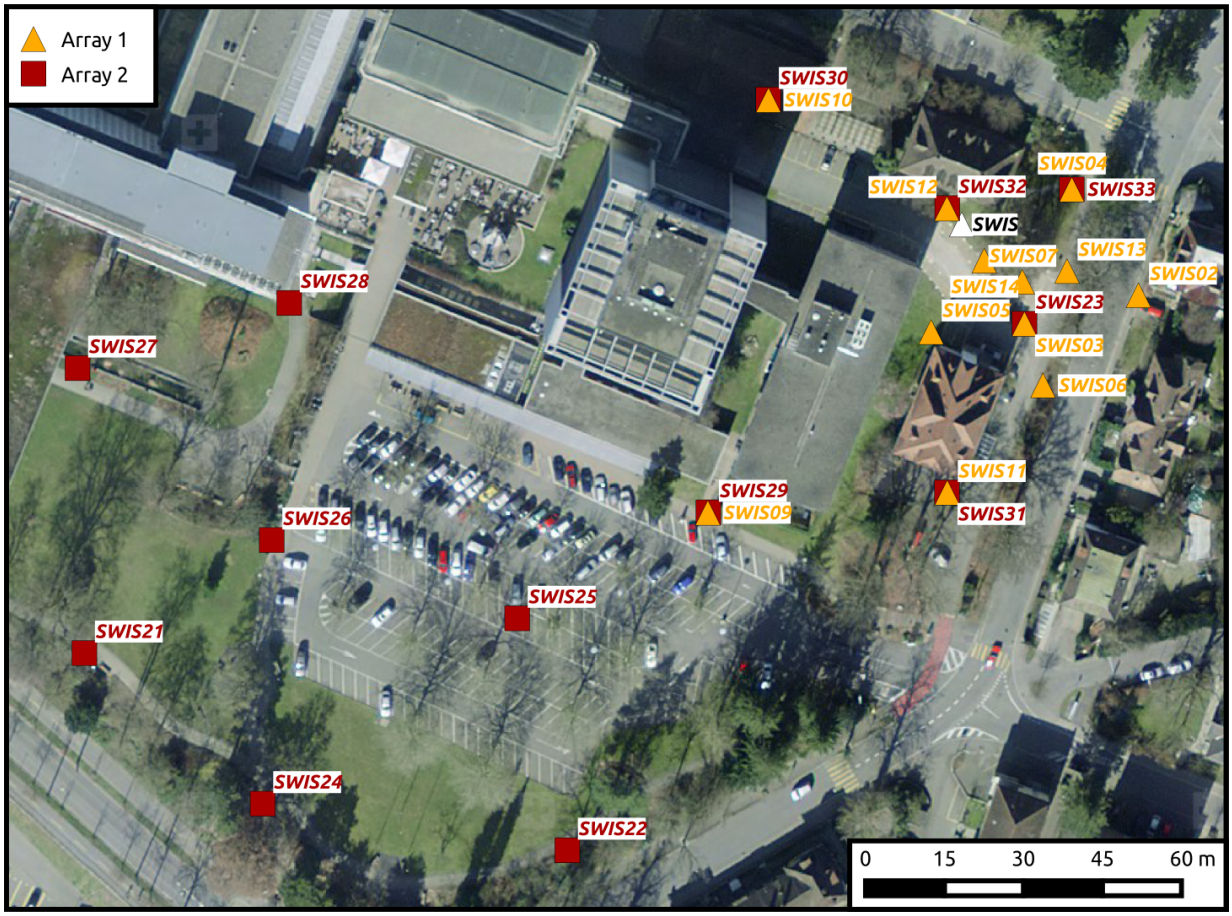


Figure 3: Layout of the array measurements around station SWIS. The location of SWIS is indicated by the white triangle, the locations of the stations during the first array measurement by orange triangles and during the second array measurement by red squares. ©2017 swisstopo (JD100042)

## 4.2 Measurement results

### 4.2.1 H/V curves

Figure 4 shows the H/V curves determined with the time-frequency analysis method (Fäh et al., 2009) for all stations of both arrays. In the small array, all stations show a consistent trough around 5 Hz. The peak of all stations only has an amplitude of only two at a frequency of around 2.5 Hz. Below this frequency, the H/V curves are mostly flat. All stations show secondary peaks at higher frequencies (between 10 and 20 Hz), but with more scattering, indicating lateral heterogeneities.
In the large array, the curves are less consistent and there is more scattering in the frequencies of the identified peaks between 1.5 and 3 Hz. Also the frequencies of the secondary peaks are more scattered in the large array.

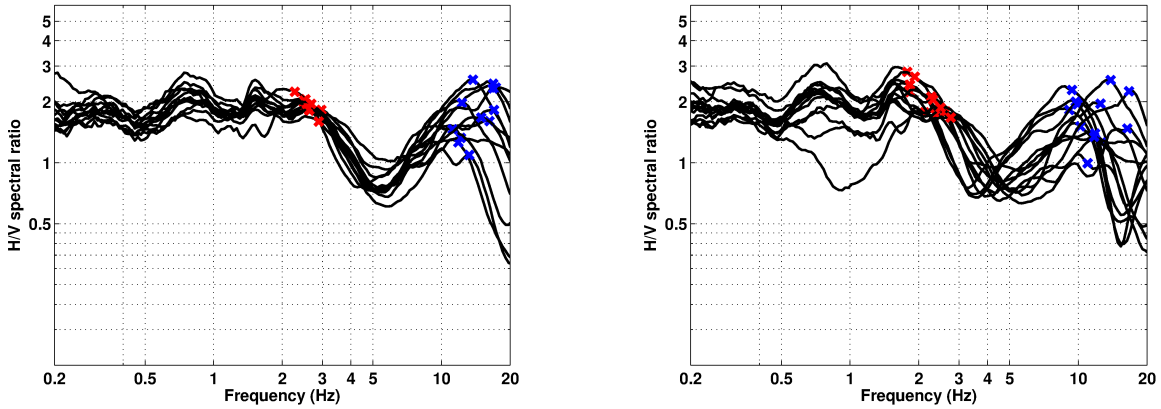


Figure 4: Overview of the H/V measurements for the different stations of first array measurement (left) and the second array measurement (right).

### 4.2.2 RayDec ellipticity curves

The RayDec technique (Hobiger et al., 2009) is meant to eliminate the contributions of other wave types than Rayleigh waves and give a better estimate of the ellipticity than the classical H/V technique. The RayDec ellipticity curves for all stations of the array measurements are shown in Fig. 5.
The results are similar to the H/V curves. Most stations in the small array have similar curves. The curve for SWIS12 is highlighted because this is the station closest to station SWIS and was therefore used as a reference here. This curve has an ellipticity peak with a peak of amplitude 2 at about 2.5 Hz. Below this frequency, there is a flat plateau down to frequencies lower than 1 Hz. Above the peak, there is a trough around 5.5 Hz. Above this trough, a secondary peak with higher amplitude at 17 Hz. This peak might correspond to a shallow interface. Other stations show this peak at different frequencies, again a sign for lateral heterogeneities.
For the large array, the curves are qualitatively comparable, but the scattering between the different curves of the different stations is larger.

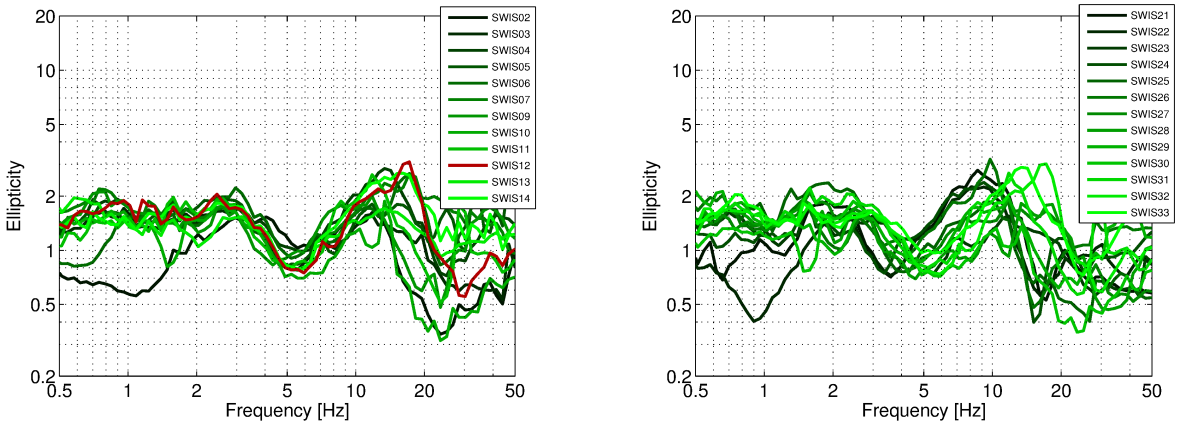


Figure 5: RayDec ellipticities for array 1 (left) and array 2 (right).

### 4.2.3 Polarization measurements

The polarization analysis according to Burjánek et al. (2010) and Burjánek et al. (2012) does not show significantly polarized particle motions for any stations of the two arrays. As an example, the polarization analysis results for station SWIS12 are shown in Fig. 6, the station closest to SWIS. There is no linear polarization visible and also no major preferred strike direction. There are no 2- or 3-dimensional wave propagation effects in the valley.

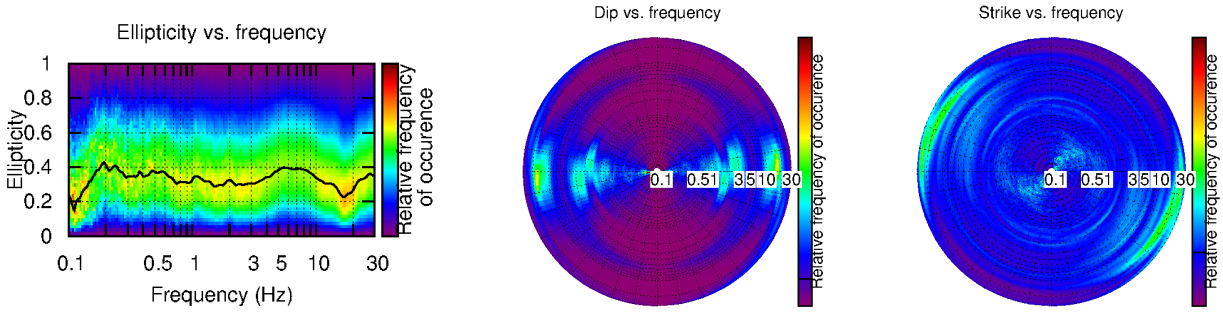


Figure 6: Polarization analysis of station SWIS12.

#### 4.2.4 3-component high-resolution FK

The results of the 3-component high-resolution FK analysis (Poggi and Fäh, 2010) of both arrays are shown in Figs 7 and 8. On the vertical component, the fundamental mode of the Rayleigh waves is clearly visible in both arrays, but only up to 20 Hz in array 1, even if the theoretical upper resolution limit is higher. Some higher modes can also be seen in array 1, but the heterogeneity between the ellipticity curves of the different stations in this frequency range questions their reliability. On the radial component, similar dispersion curves can be retrieved in both arrays. The curves of the vertical and radial components seem compatible.
On the transverse component, the fundamental Love wave dispersion curve is well identified in both arrays, but the high-frequency theoretical array resolution limits cannot be completely reached. Array 2 shows a higher mode.
The ellipticity curves determined with the 3-component HRFK analysis are shown in Fig. 8.

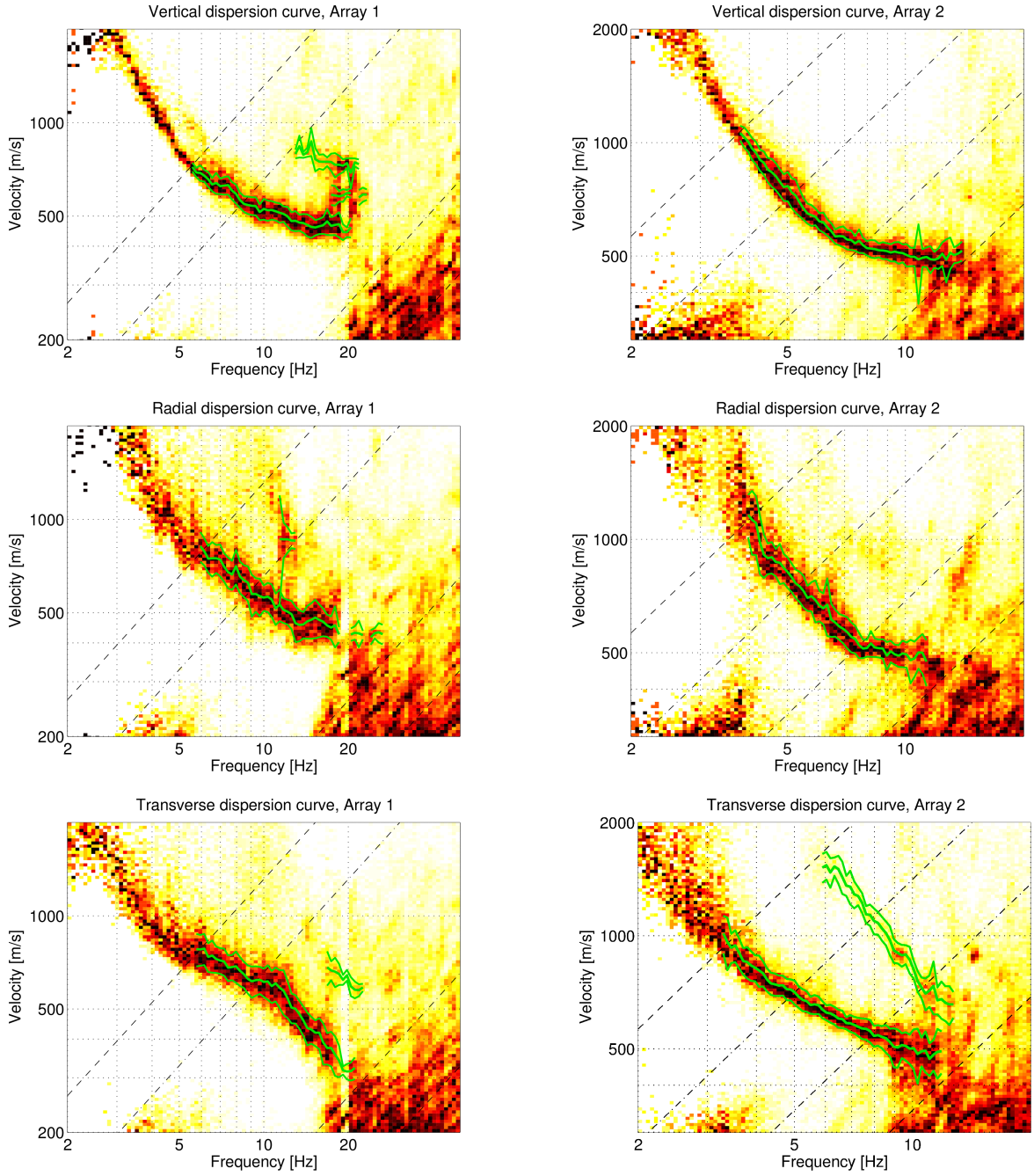


Figure 7: Dispersion curves obtained with the 3-component HRFK algorithm (Poggi and Fäh, 2010). In the left column, the results for array 1 are shown, in the right column for array 2. The lines from top to bottom show the results for the vertical, radial and transverse components, respectively. The dashed and dotted black lines are the array resolution limits. The solid green lines are picked from the data, where the central line indicates the best values and the two outer lines the standard deviation.

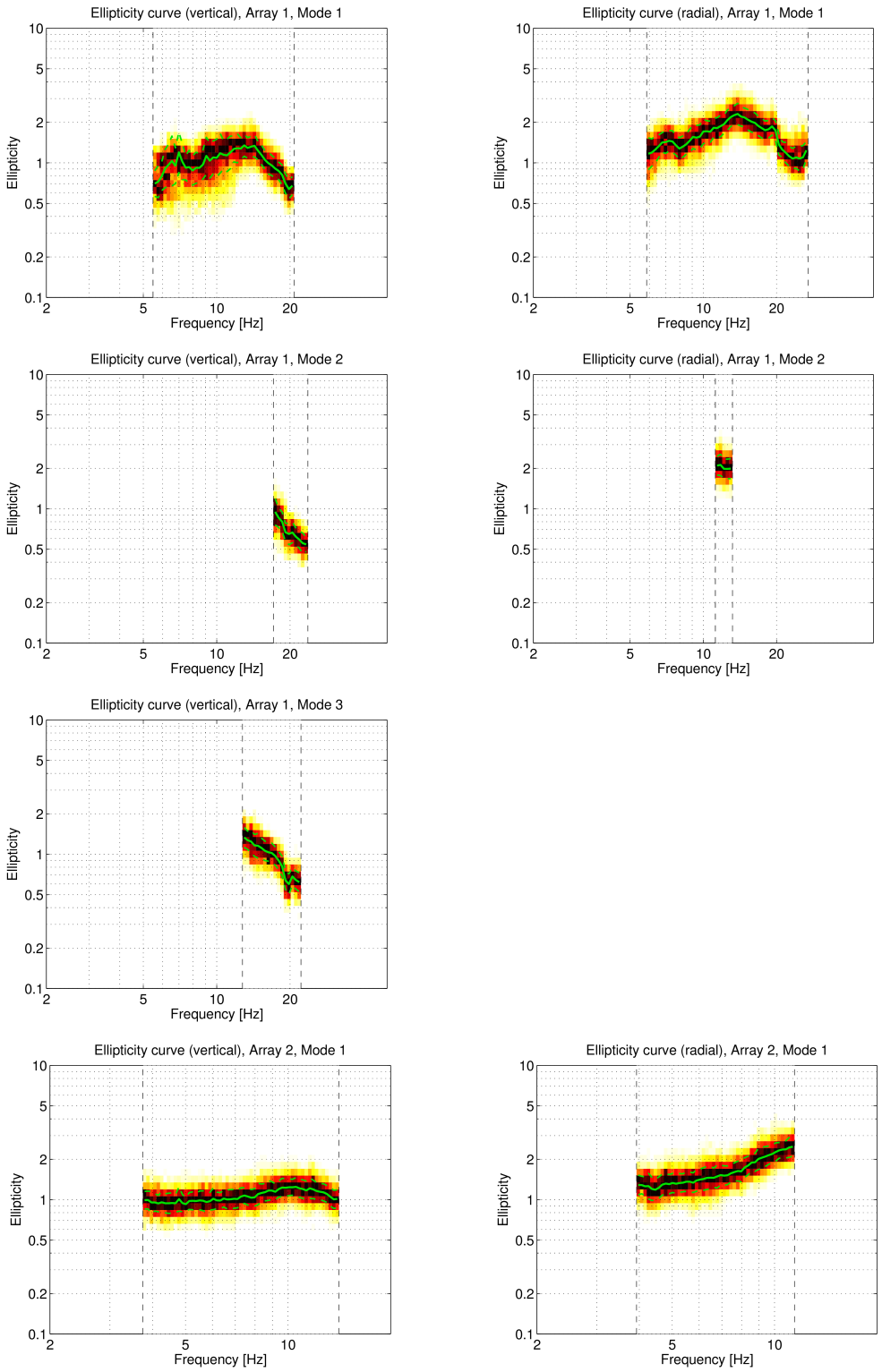


Figure 8: Ellipticity curves obtained with the 3-component HRFK algorithm (Poggi and Fäh, 2010) for the vertical component (left) and the radial component (right). The frequency ranges of the different curves correspond to the ranges where the dispersion curves had been picked.

### 4.2.5 WaveDec

The results of the WaveDec (Maranò et al., 2012) processing are shown in Figs 9 and 10. We applied the technique with the option to model three wave contributions simultaneously, tuning the code with a $\gamma$ value of 0.2 to rely more on the Maximum Likelihood approach than on the Bayesian Information Criterion.
As can be seen in Fig. 9, the Love waves are better retrieved in array 2, but still with good quality in array 1. The Rayleigh wave dispersion curve is also well retrieved in both arrays. The theoretical array resolution limits are not always reached.
The ellipticity curves in Fig. 10 are plotted in two ways. On the left side, the ellipticity angle is shown. On the right side, the ellipticity itself is shown. The WaveDec code actually estimates the ellipticity angle. Ellipticity is the absolute value of the tangent of this angle. A negative ellipticity angle stands for retrograde particle motion, a positive ellipticity angle for prograde particle motion.
The ellipticity is retrograde over the whole resolved frequency range, but there are signs that it changes to prograde at higher frequencies.

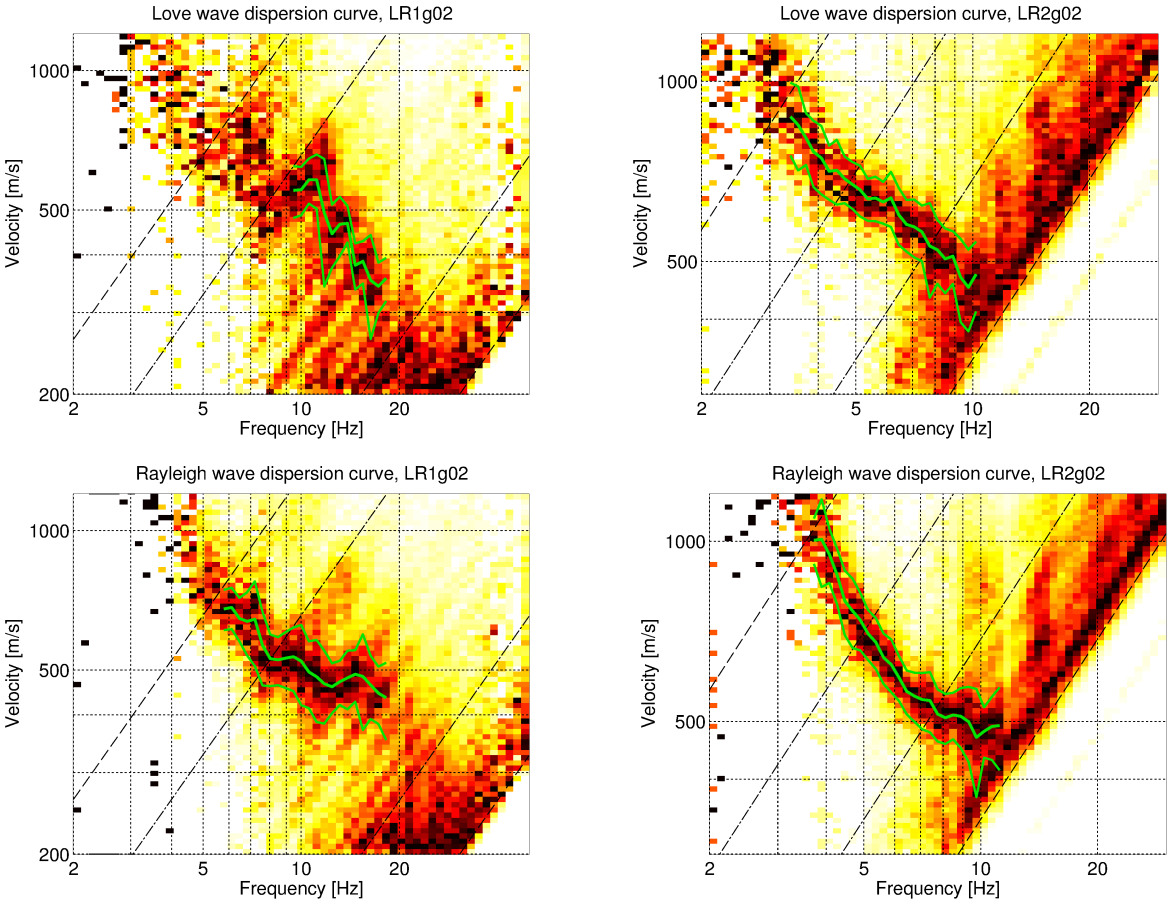


Figure 9: Love (top) and Rayleigh (bottom) wave dispersion curves obtained with the WaveDec technique (Maranò et al., 2012). The dashed lines indicate the theoretical array resolution limits.

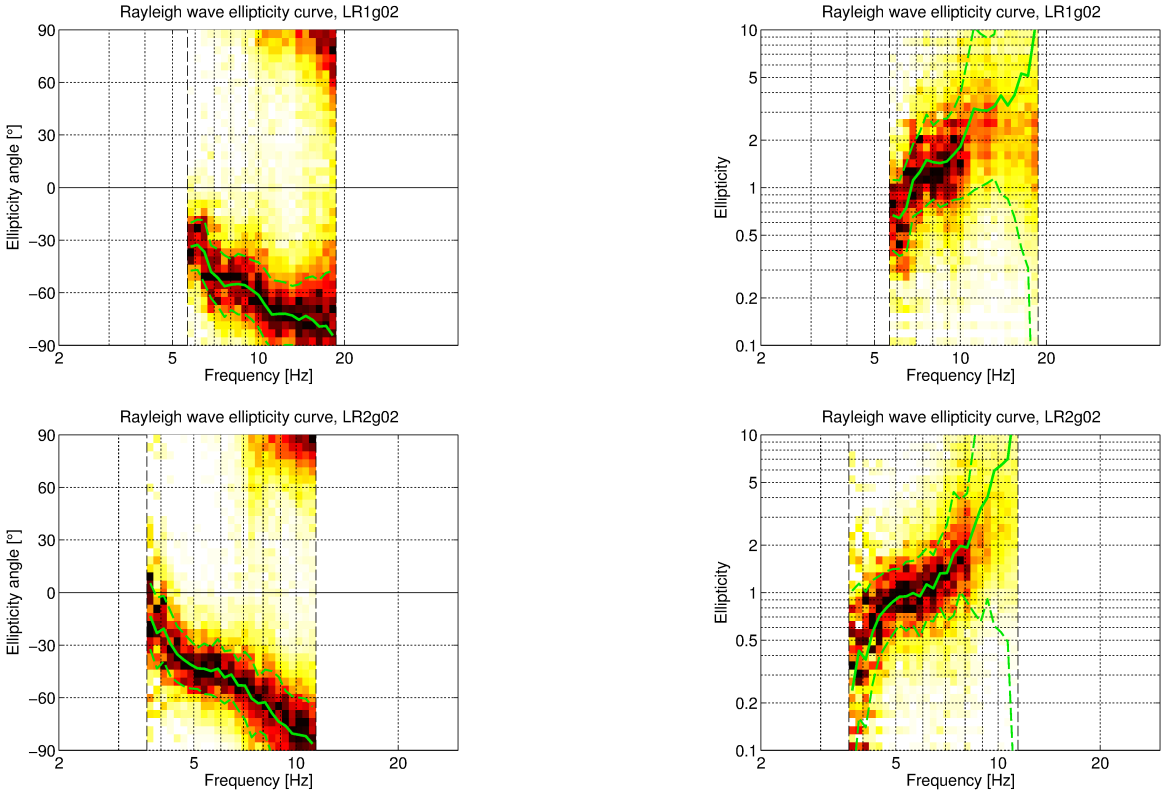


Figure 10: Rayleigh wave ellipticity curves obtained with the WaveDec technique (Maranò et al., 2012) for both arrays. The left column shows the ellipticity angles, the right column the tangent of this angle, i.e. the ellipticity. The different rows correspond to the different array configurations.

### 4.2.6 SPAC

For both arrays, we also calculated the SPAC (Aki, 1957) curves of the vertical components, using the M-SPAC (Bettig et al., 2001) technique implemented in geopsy. Rings with different radius ranges have been defined. For all station pairs with distance inside this radius range, the cross-correlation is calculated in different frequency ranges. These cross-correlation curves are averaged for all station pairs of the respective ring and give the SPAC curve. The rings are defined in such a way that at least three station pairs contribute and that their connecting vectors have a good directional coverage.
The SPAC curves for all defined rings are shown in Figs 11 and 12, respectively. The black points indicate the data values which contributed to the final dispersion curve estimation, which was made with the function `spac2disp` of the geopsy package. These resulting dispersion curves are shown in Fig. 13. For array 1, the dispersion curve is retrieved between 2.7 and 12.2 Hz. For array 2, it is retrieved between 2.3 and 8.0 Hz.

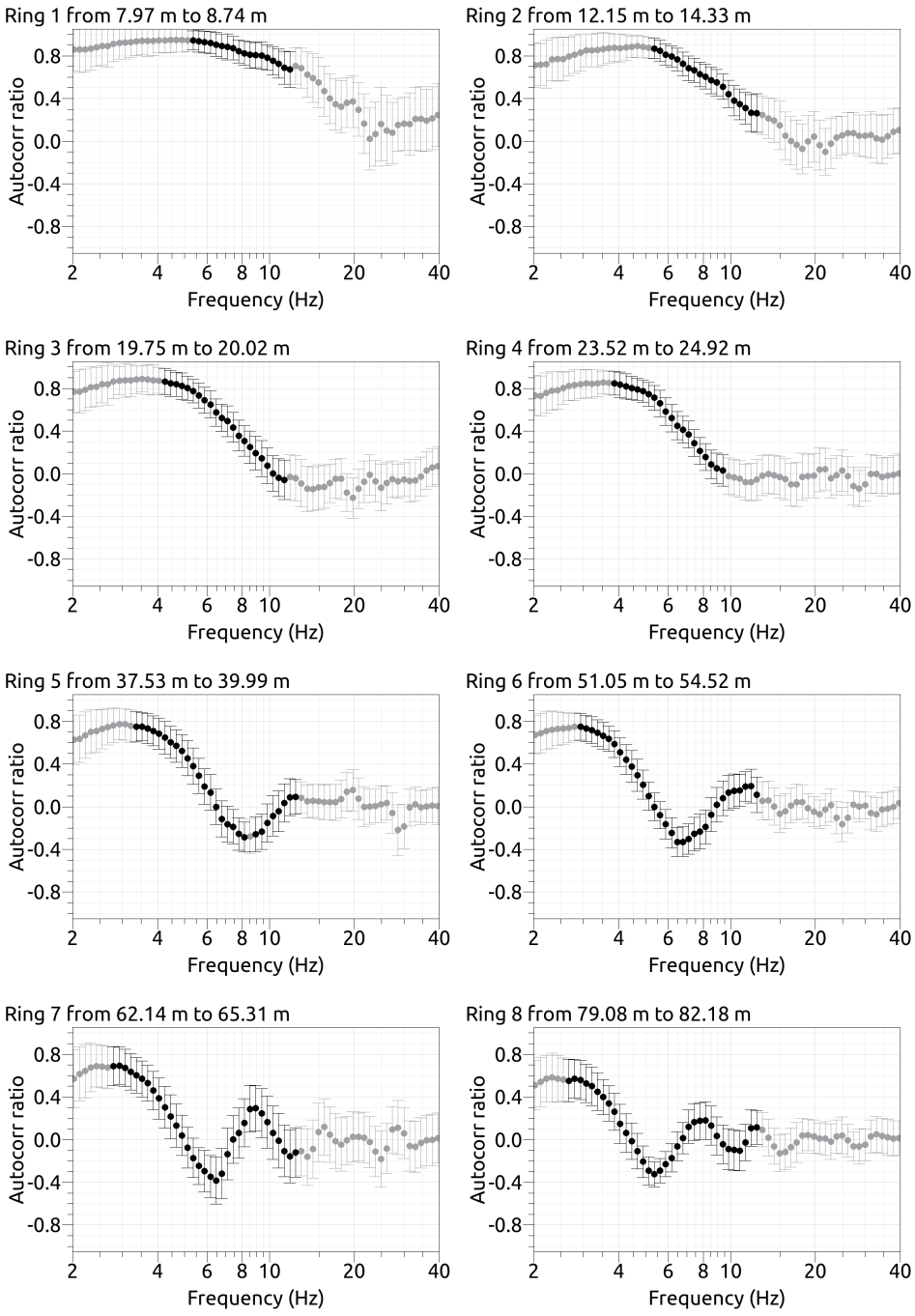


Figure 11: SPAC curves for array 1. The black data points contributed to the dispersion curve estimation.

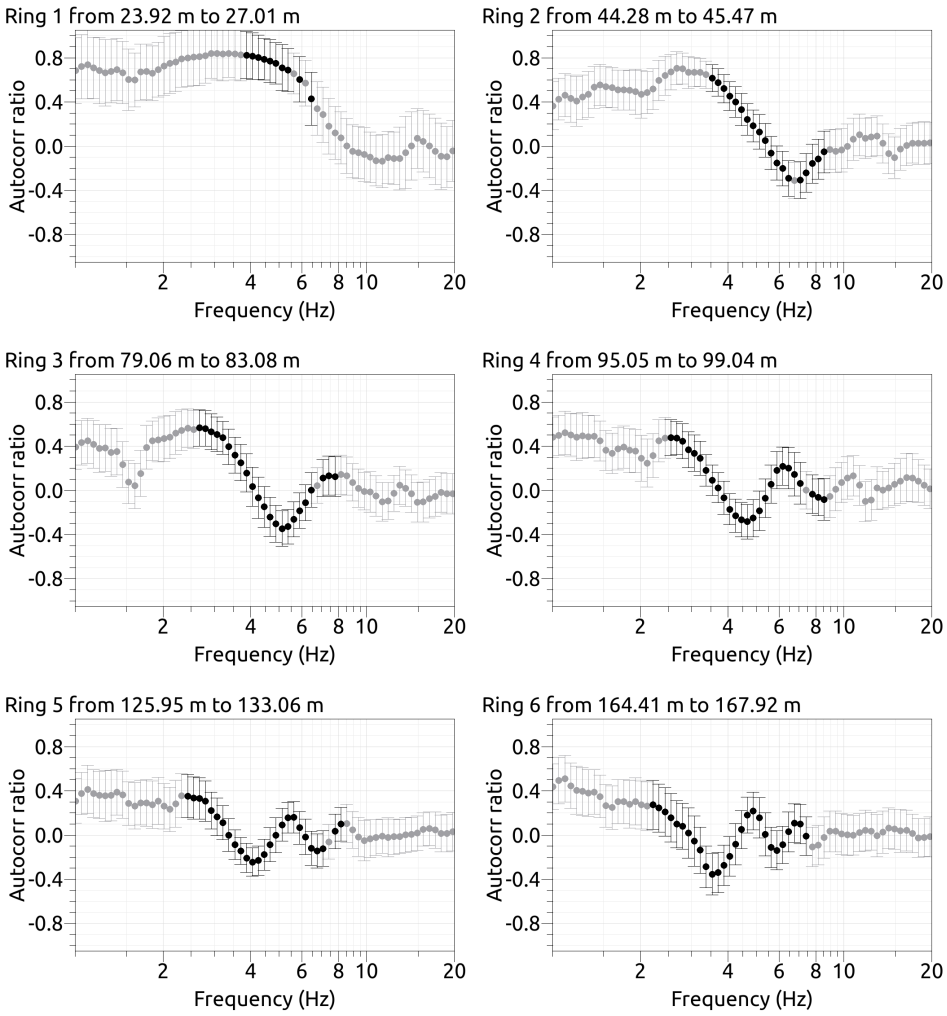


Figure 12: SPAC curves for array 2. The black data points contributed to the dispersion curve estimation.

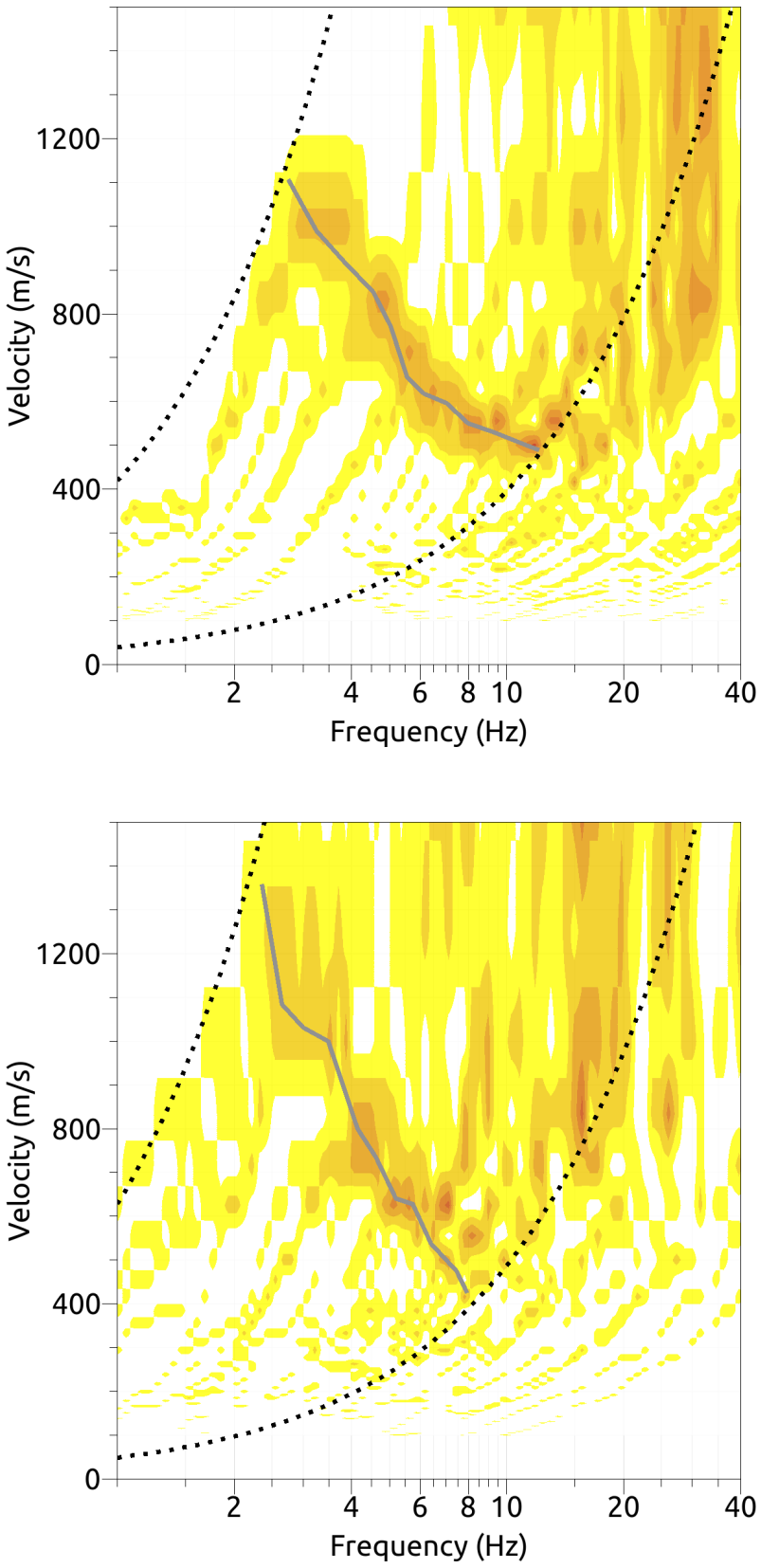


Figure 13: Resulting Rayleigh wave velocities for array 1 (top) and array2 (bottom). The gray line corresponds to the picked dispersion curve. The black curves are resolution limits, which are different from the FK analysis resolution limits.

## 4.3 Summary

Fig. 14 gives an overview of the dispersion and ellipticity curves determined by the different methods. The results of both arrays are different for the Love waves, even if the different methods give similar curves for each array. In the intermediate frequency range, the larger array measured lower velocities for Love waves than the small array, but the high-frequency dispersion curve from the small array is compatible with the large array's curve. With both arrays, higher modes are visible. The shift of the dispersion curves for both arrays may be caused by different interface depths at both locations.
For the Rayleigh waves, the results from both arrays are in better agreement and all methods give very similar curves. For the ellipticity curves, the singularities that can be guessed from the WaveDec results are not compatible with the RayDec ellipticity curve, which does not show any signs for singularities. Anyhow, the results of the array methods are limited by the lower array resolution limits, so that they do not give results around the broad peak of the RayDec curve.

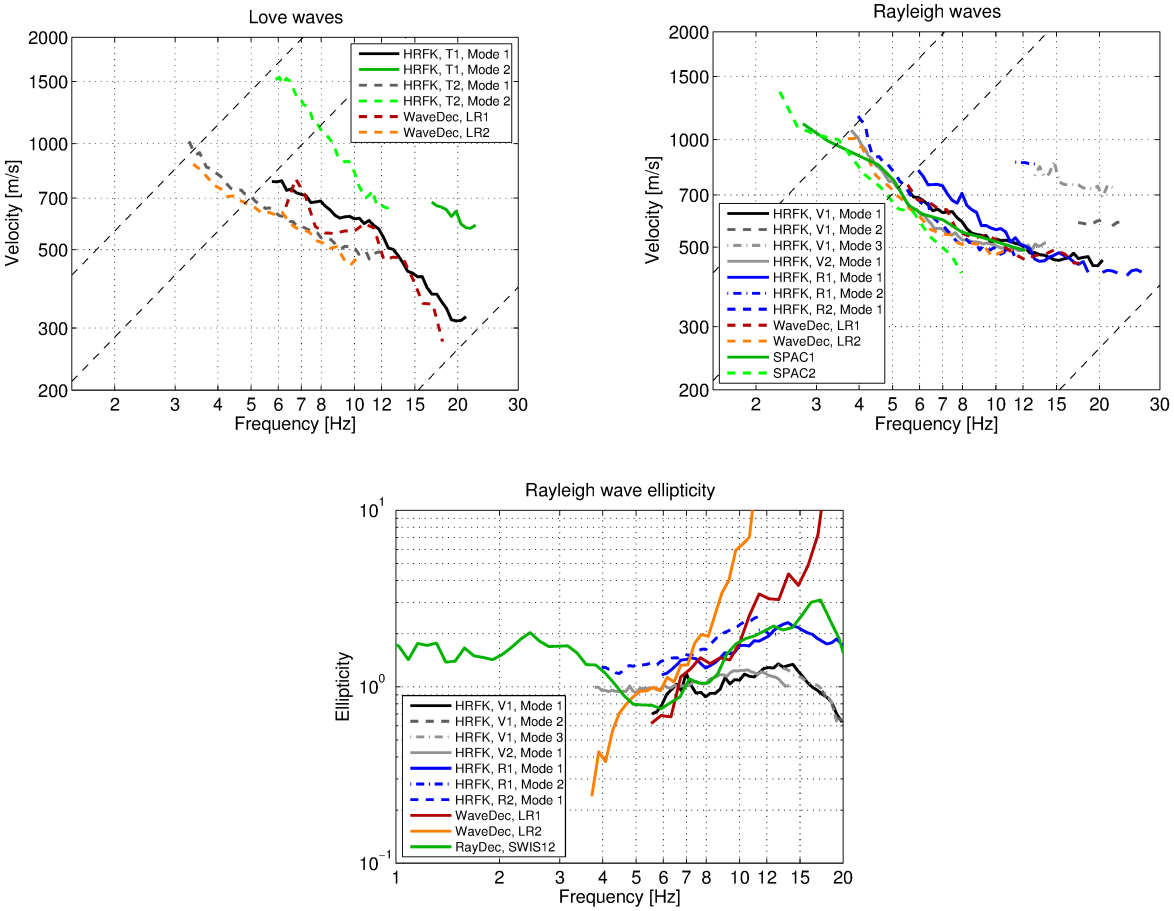


Figure 14: Overview of the Love and Rayleigh wave dispersion curves as well as the ellipticity curves for both arrays. The dashed lines indicate the theoretical resolution limits of the respective arrays (the upper frequency limits corresponds to array 1, the lower one to array 2). The RayDec ellipticity curve corresponds to station SWIS12, the closest station to SWIS.

# 5 Data inversion

## 5.1 Inversion targets

For the Love waves, we decided to trust the larger array more than the smaller one. Therefore, its dispersion curve (determined by HRFK) was used, combined with some data points from the small array at higher frequency. For the Rayleigh wave dispersion curves, we also used more data from the large than the small array, only complementing the large array at higher frequencies. For the ellipticity, the broad peak and some data from higher frequencies were used. The data curves that have been used for the inversion are indicated in Table 2 and are shown in Fig. 15.

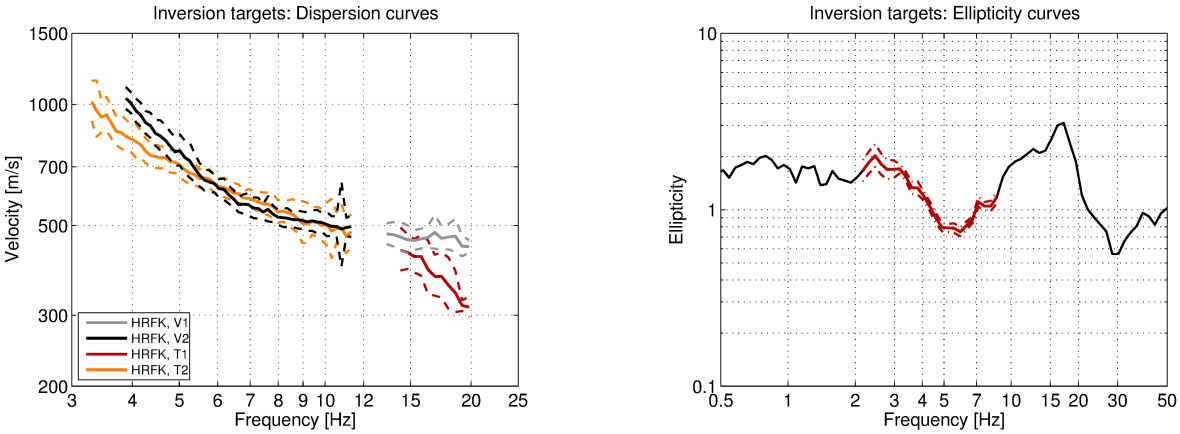


Figure 15: Overview of the dispersion and ellipticity curves used as targets for the different inversions.

Table 2: List of the data curves used as targets in the inversions.

| Array | Method | Wave type | Mode | Curve type | Frequency range [Hz] |
|---|---|---|---|---|---|
| 1 | HRFK (V) | Rayleigh | fundamental | dispersion | 13.1 - 19.7 |
| 2 | HRFK (V) | Rayleigh | fundamental | dispersion | 3.9 - 11.3 |
| 1 | HRFK (T) | Love | fundamental | dispersion | 14.2 - 19.7 |
| 2 | HRFK (T) | Love | fundamental | dispersion | 3.3 - 11.3 |
| 1 | RayDec (SBAS12) | Rayleigh | fundamental | ellipticity | 2.1 - 8.9 |

## 5.2 Inversion results

Using the dinver code of the geopsy package (Wathelet et al., 2004), we performed six inversions with different parameterizations, ranging from 4 to 8 layers and using a fixed-depth approach (see Table 3). Each inversion run produced 200 000 total models in order to assure a good convergence of the solution. The results of these inversions are shown in Figs. 16 - 21.
All inversions yield very similar minimum misfit values, they are slightly larger for the models with more parameters. The data are fitted in a similar way in all inversions. Only the Love wave dispersion curve at frequencies below 4 Hz is not well fitted and all inversions produce systematically lower velocities.
As a result, all inversions produce acceptable solutions.

Table 3: List of inversions

| Inversion | Number of layers | Number of models | Minimum misfit |
|---|---|---|---|
| SWIS4l | 4 | 200 000 | 0.620 |
| SWIS5l | 5 | 200 000 | 0.625 |
| SWIS6l | 6 | 200 000 | 0.651 |
| SWIS7l | 7 | 200 000 | 0.663 |
| SWIS8l | 8 | 200 000 | 0.684 |
| SWISfix | 18 | 200 000 | 0.694 |

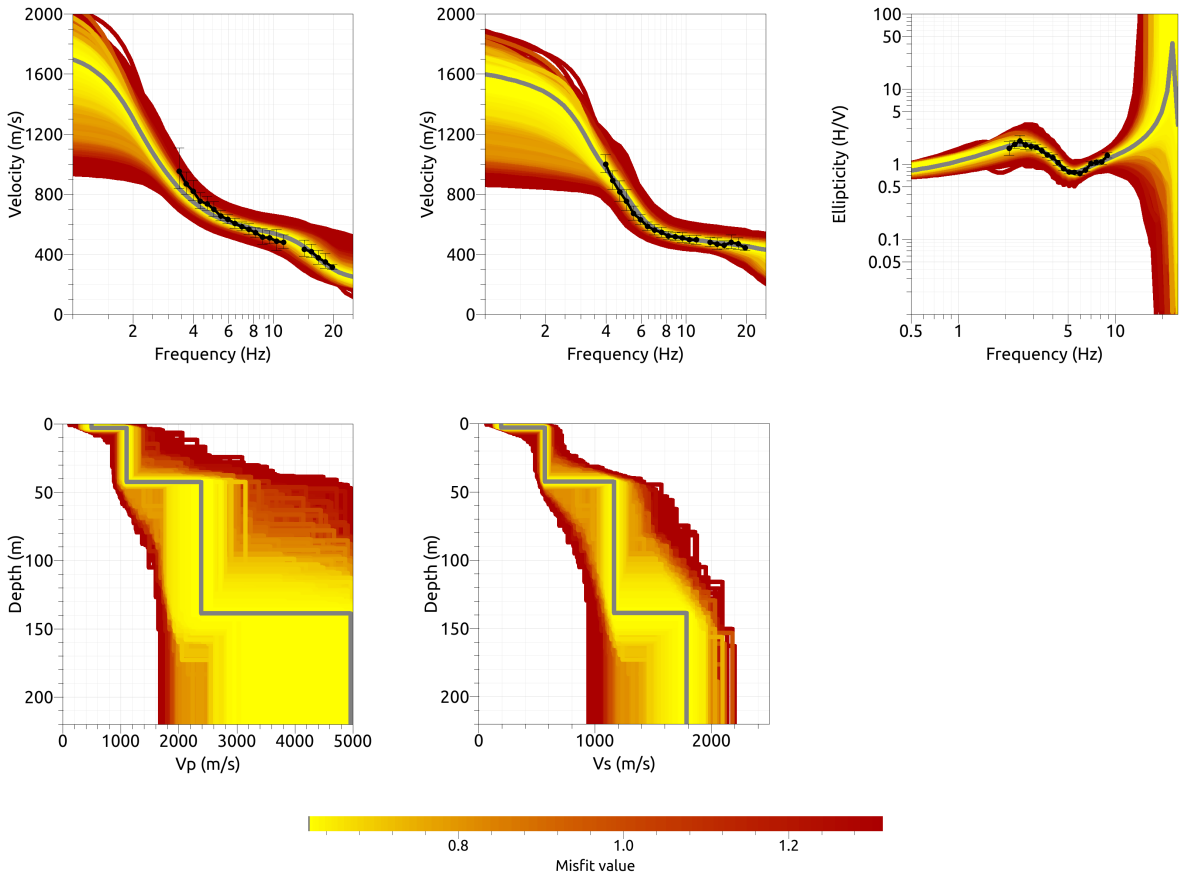


Figure 16: Inversion : Love wave fundamental mode dispersion curve (top left), Rayleigh wave fundamental mode dispersion curve (top center), Rayleigh wave ellipticity curve (top right), P-wave velocity profiles (center left) and S-wave velocity profiles (center right). The black dots indicate the data points used for the inversion, the gray line indicates the best-fitting model.

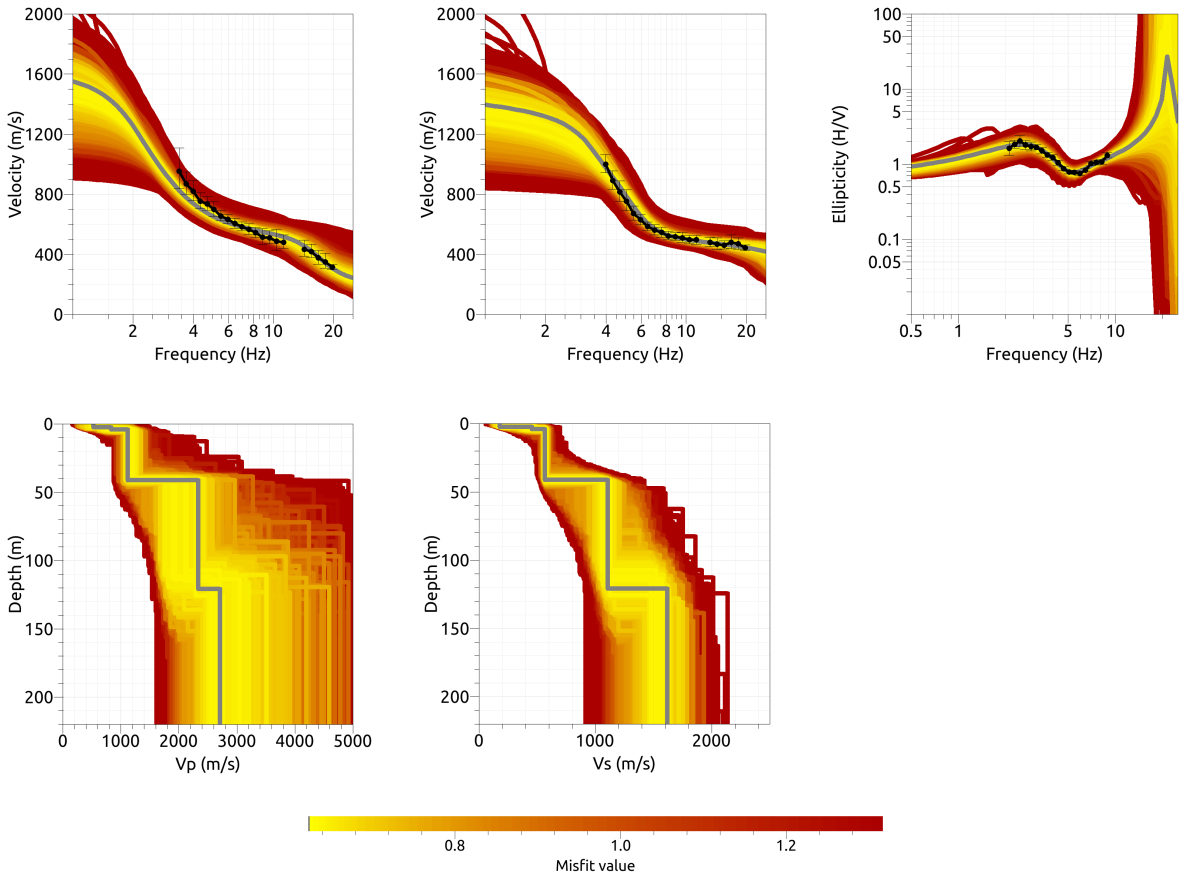


Figure 17: Inversions SWIS4l (top) and SWIS5l (bottom): Love wave fundamental mode dispersion curve (top left), Rayleigh wave fundamental mode dispersion curve (top center), Rayleigh wave ellipticity curve (top right), P-wave velocity profiles (center left) and S-wave velocity profiles (center right). The black dots indicate the data points used for the inversion, the gray line indicates the best-fitting model.

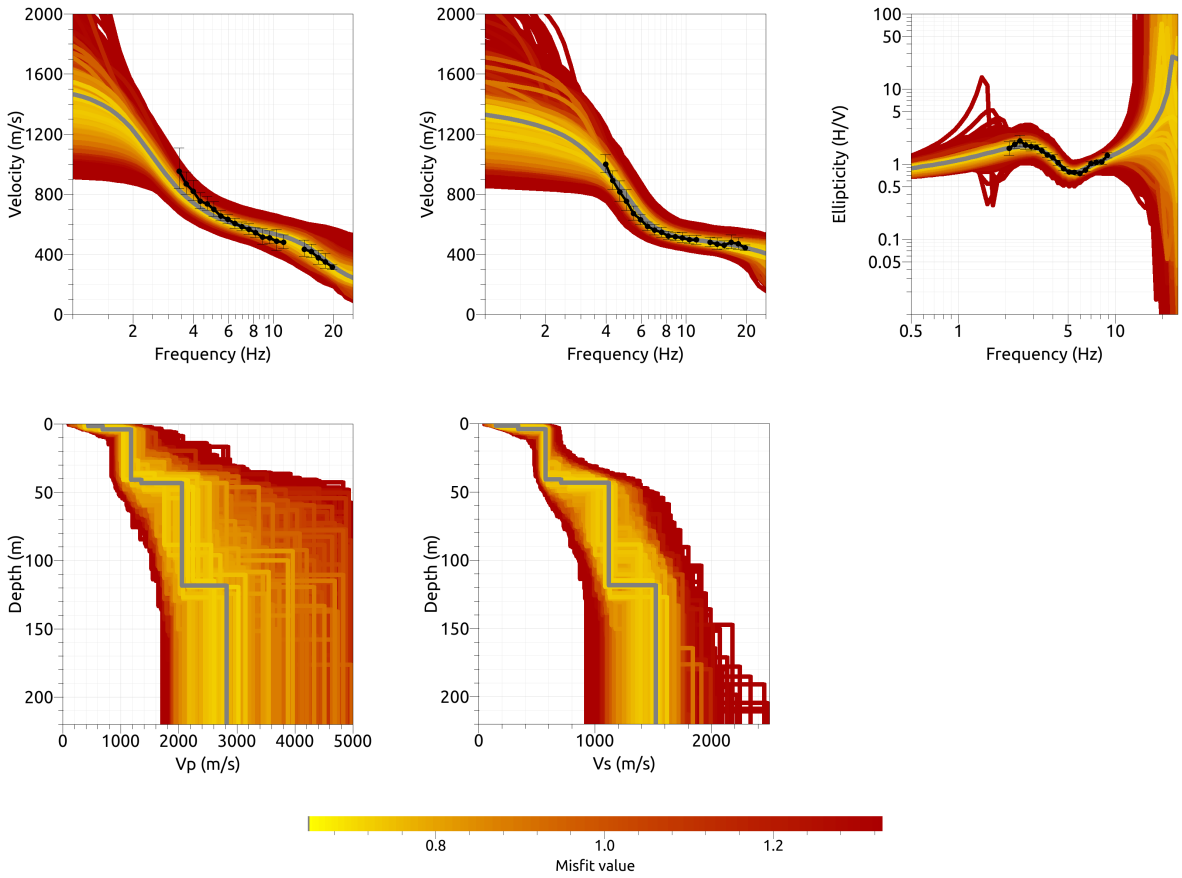


Figure 18: Inversion SWIS6l: Love wave fundamental mode dispersion curve (top left), Rayleigh wave fundamental mode dispersion curve (top center), Rayleigh wave ellipticity curve (top right), P-wave velocity profiles (center left) and S-wave velocity profiles (center right). The black dots indicate the data points used for the inversion, the gray line indicates the best-fitting model.

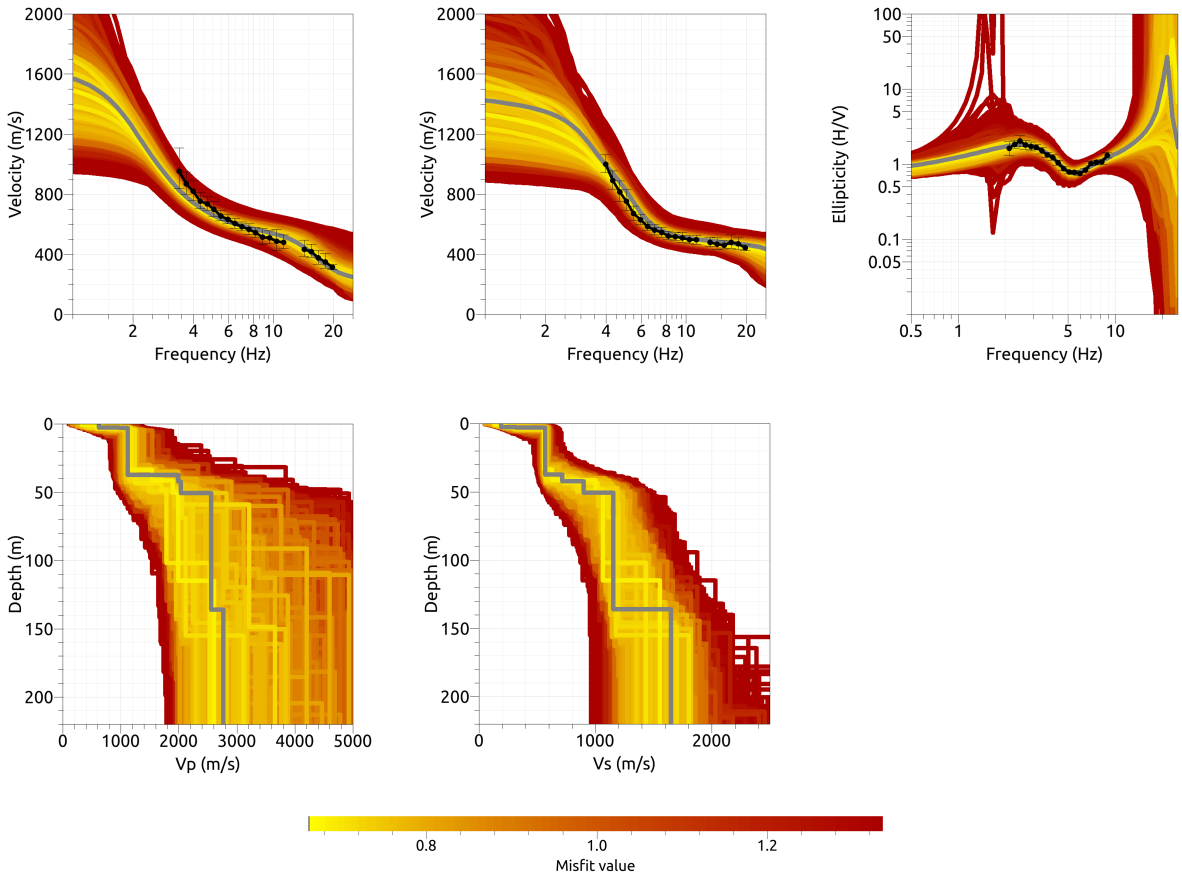


Figure 19: Inversion SWIS7l: Love wave fundamental mode dispersion curve (top left), Rayleigh wave fundamental mode dispersion curve (top center), Rayleigh wave ellipticity curve (top right), P-wave velocity profiles (center left) and S-wave velocity profiles (center right). The black dots indicate the data points used for the inversion, the gray line indicates the best-fitting model.

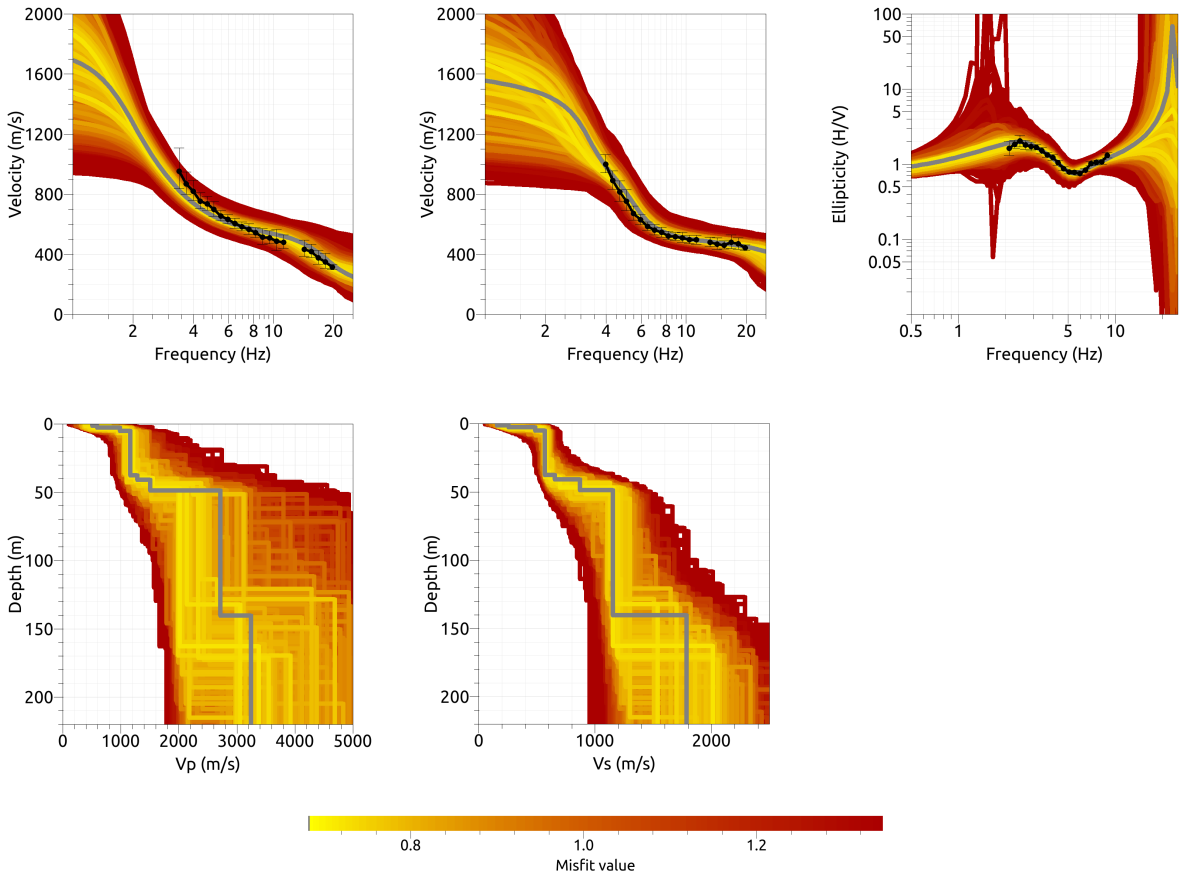


Figure 20: Inversion SWIS8l: Love wave fundamental mode dispersion curve (top left), Rayleigh wave fundamental mode dispersion curve (top center), Rayleigh wave ellipticity curve (top right), P-wave velocity profiles (center left) and S-wave velocity profiles (center right). The black dots indicate the data points used for the inversion, the gray line indicates the best-fitting model.

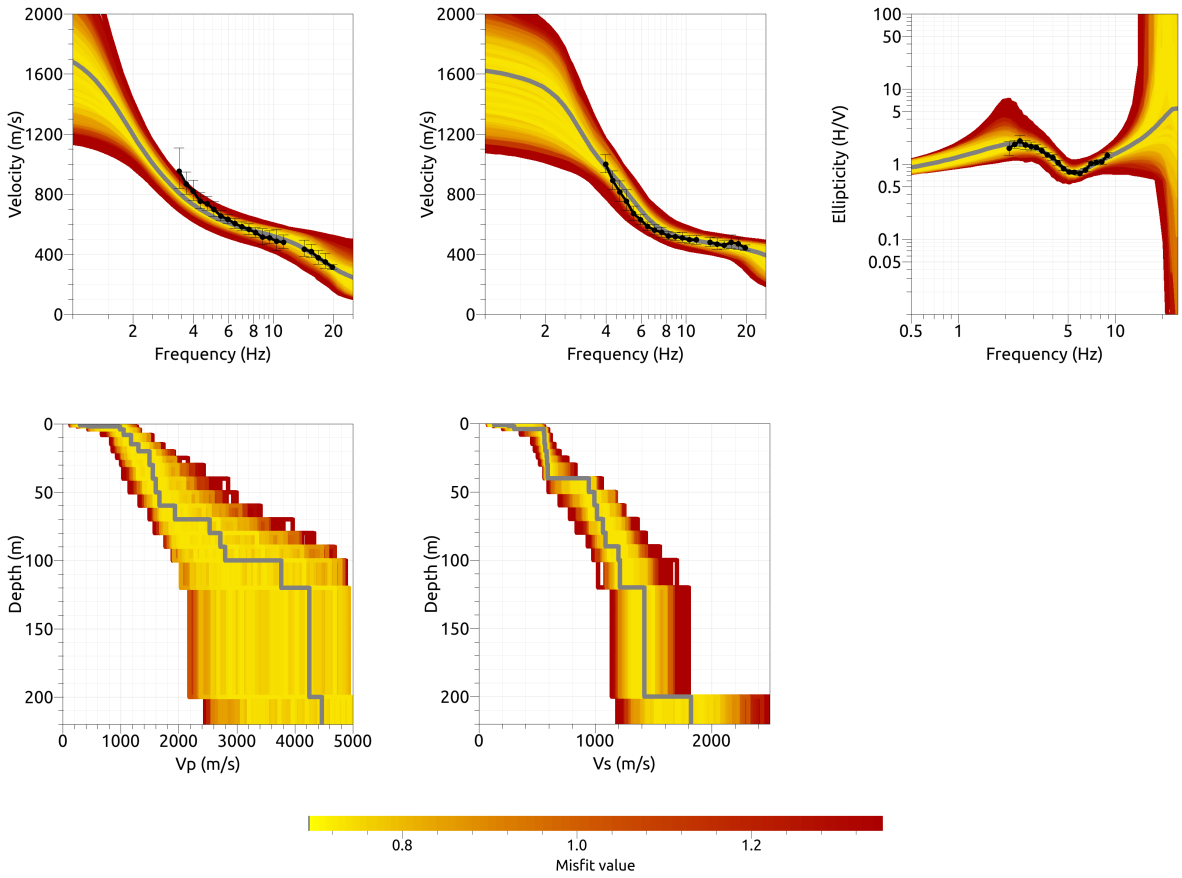


Figure 21: Inversion SWISfix: Love wave fundamental mode dispersion curve (top left), Rayleigh wave fundamental mode dispersion curve (top center), Rayleigh wave ellipticity curve (top right), P-wave velocity profiles (center left) and S-wave velocity profiles (center right). The black dots indicate the data points used for the inversion, the gray line indicates the best-fitting model.

## 5.3 Discussion of the inversion result

The best-fitting models of all inversions are shown in Fig. 22. There are some differences between the different parameterizations, mainly caused by the different number of parameters. But overall, the resulting velocity profiles can be quite well described using only four layers and are very consistent in the superficial part. The shallowest layer has a shear-wave velocity of about 180 m/s and a depth of 2 to 4 m. The second layer, reaching to a depth of about 40 m, has a velocity of roughly 570 m/s. The following structure has a shear-wave velocity between 1100 and 1200 m/s and reaches about 120 to 140 m deep, where the seismic bedrock with velocities above 1500 m/s starts.
From a borehole at the hospital site, there is an indication of marl layer at 36 m. This would be consistent with our inversion results. Therefore, we interpret the first layers of 2 to 4 m thickness as unconsolidated sediments, followed by quaternary sediments down to 40 m, where the marl starts. The interface between the quaternary sediments and the marl produces the observed H/V peak.
The average $V_{S30}$ value of the best-fitting models for all inversions is $478 \pm 4\, m/s$, corresponding to class B (EC8) or class C (SIA261).

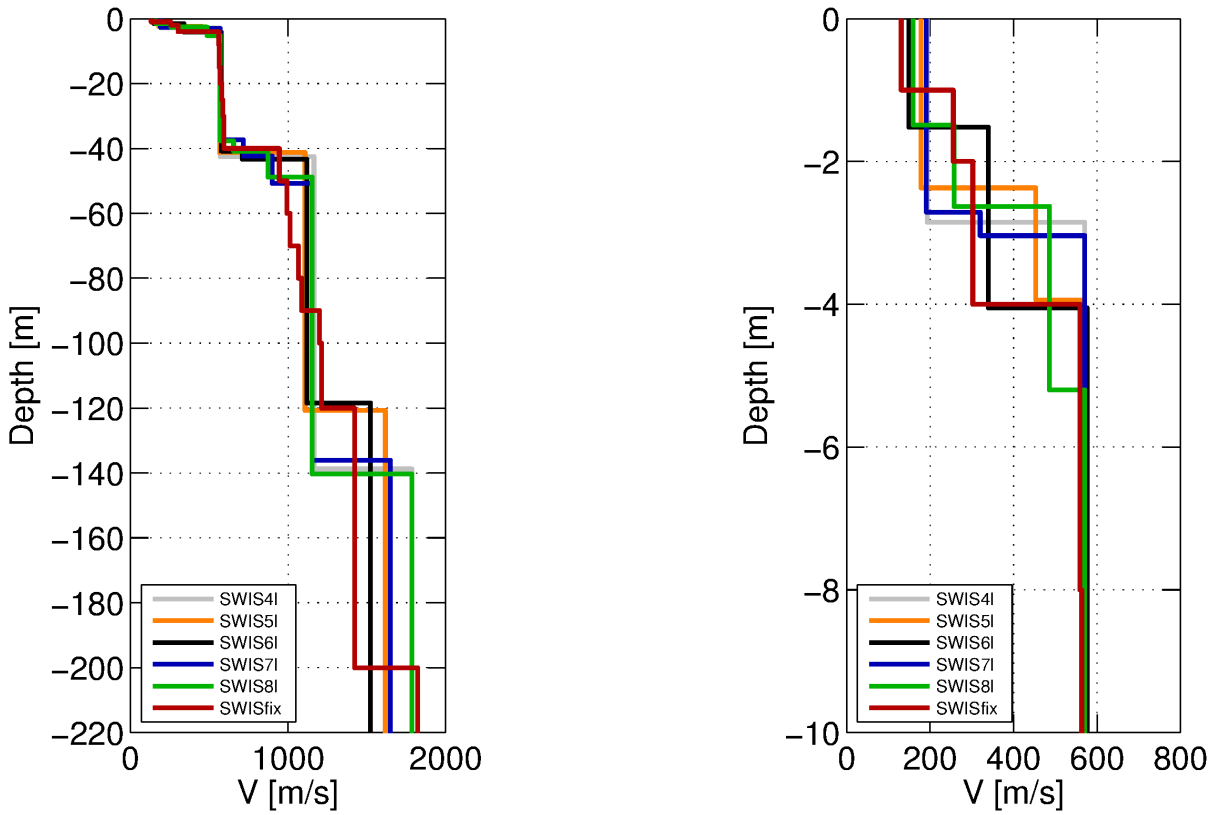


Figure 22: Overview of shear-wave velocity profiles of the best-fitting models of all inversions (left) and a zoom on the superficial layers (right).

## 5.4 SH transfer function

The empirical amplification for station SWIS is based on only three events so far, but it fits the modeled SH wave amplification at the site quite well, especially between 1 and 5 Hz (Fig. 23). At higher frequencies, the empirical amplification is shifted to higher values than the modeled one, but the peak frequencies are in good agreement.

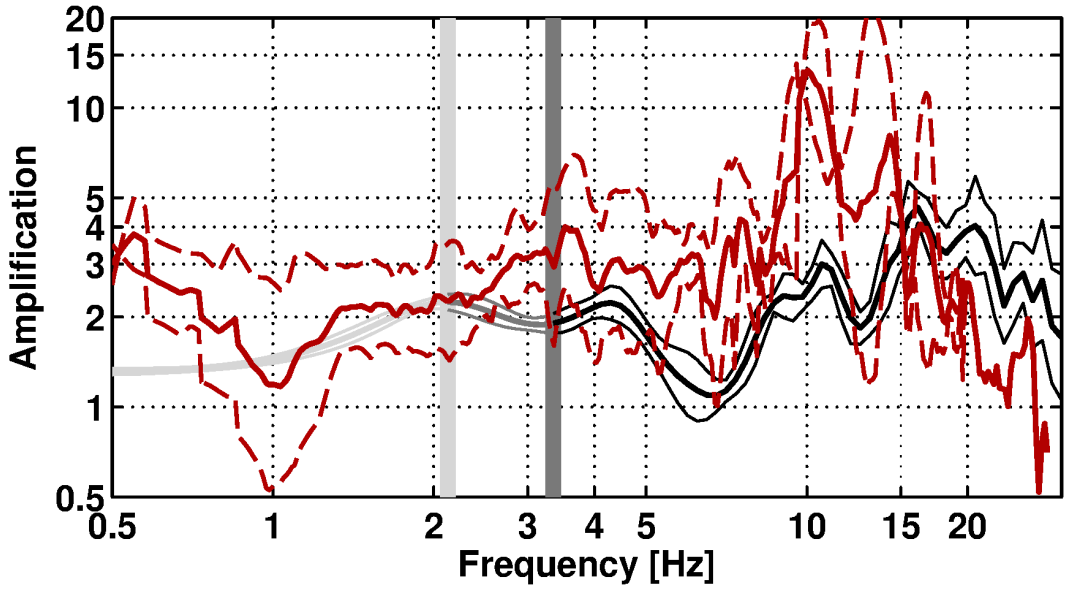


Figure 23: Comparison between the modeled amplification for the best models of the six different inversions (black, with standard deviation) and the empirical amplification measured at station SWIS (red, with standard deviation).

## 5.5 Quarter-wavelength representation

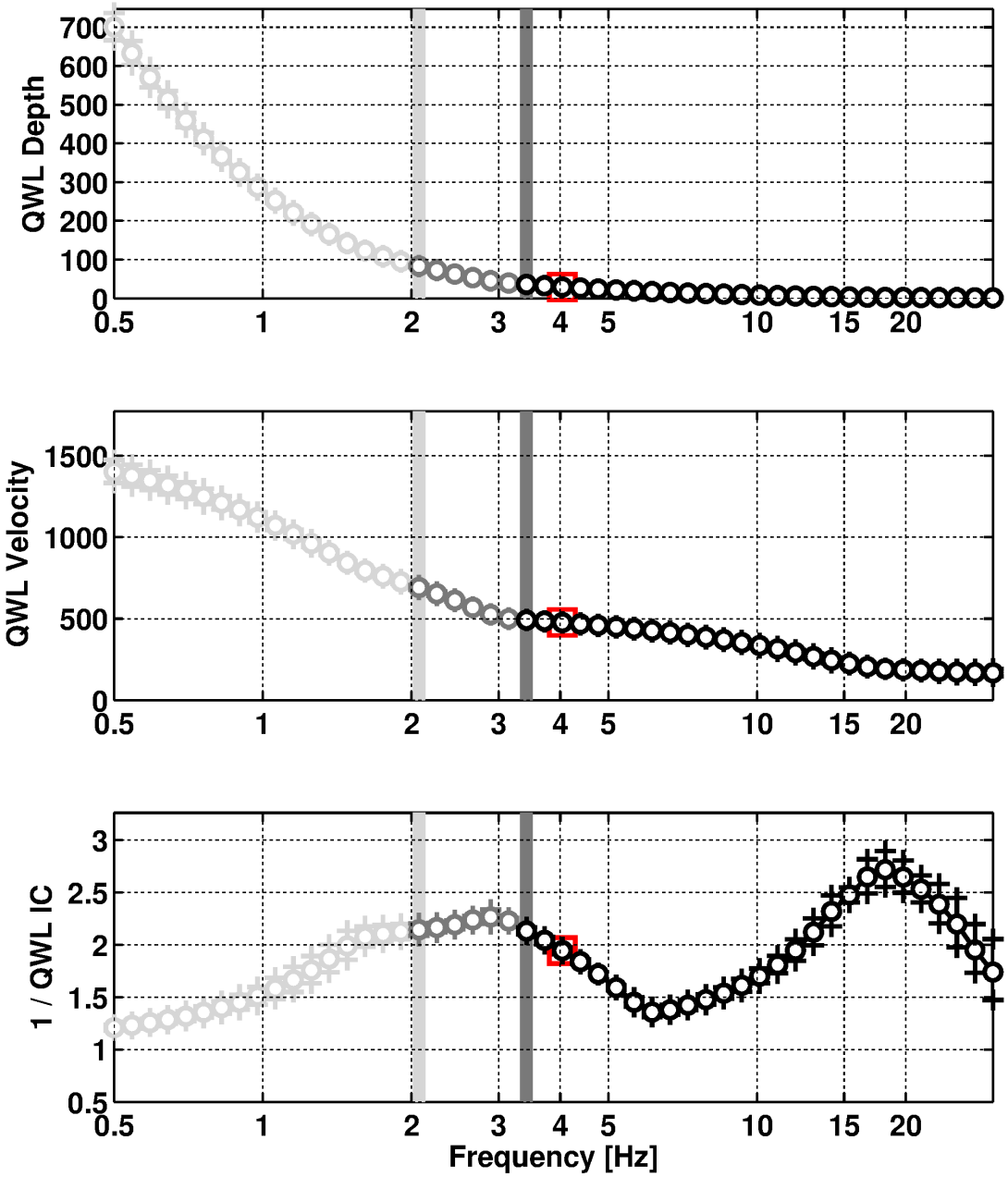


Figure 24: Quarter wavelength representation of the velocity profile for the best models of the five inversions with at least four layers (top: depth, center: velocity, bottom: inverse of the impedance contrast). The black curves are constrained by the dispersion curves, the light grey curves are not constrained by the data. The red square corresponds to $V_{S30}$.

# 6 Conclusion

We performed a passive array measurement with two different configurations to characterize the underground under station SWIS in Winterthur (ZH).
Combining both arrays, the dispersion curves for both fundamental Love and Rayleigh waves could be measured well over a wide frequency range. The ellipticity of the fundamental Rayleigh wave mode was also measured. It does not show singularities, but consists of a rather broad and flat fundamental peak.
The joint inversion of Love and Rayleigh wave dispersion curve and the ellipticity curve showed that the underground S-wave velocity profile can be described by a first superficial layer of around 2 to 4 m thickness with an S-wave velocity of around 180 m/s, followed by a second layer of around 570 m/s down to about 40 m. A third layer of around 1150 m/s follows down to a depth of at least 120 m, where the seismic bedrock is. These layers would correspond to unconsolidated sediments in the first layer, followed by quaternary sediments down to about 40 m, where a marl layer starts and is responsible for the H/V peak.
The $V_{S30}$ of the best models is about 480 m/s, corresponding to soil class B (EC8) or C (SIA261).

# Acknowledgements

The authors thank Oona Brunner and Dylan Longridge for their help during the array measurements.

# References


Aki, K. (1957). Space and time spectra of stationary stochastic waves, with special reference to microtremors. *Bull. Earthquake Res. Inst. Tokyo Univ.*, 35:415–456.

Bettig, B., Bard, P.-Y., Scherbaum, F., Riepl, J., Cotton, F., Cornou, C., and Hatzfeld, D. (2001). Analysis of dense array noise measurements using the modified spatial auto-correlation method (SPAC): application to the Grenoble area. *Boll. Geof. Teor. Appl.*, 42:281–304.

Burjánek, J., Gassner-Stamm, G., Poggi, V., Moore, J. R., and Fäh, D. (2010). Ambient vibration analysis of an unstable mountain slope. *Geophys. J. Int.*, 180:820–828.

Burjánek, J., Moore, J. R., Molina, F. X. Y., and Fäh, D. (2012). Instrumental evidence of normal mode rock slope vibration. *Geophys. J. Int.*, 188:559–569.

Fäh, D., Wathelet, M., Kristekova, M., Havenith, H., Endrun, B., Stamm, G., Poggi, V., Burjanek, J., and Cornou, C. (2009). Using ellipticity information for site characterisation. NERIES deliverable JRA4 D4, available at http://www.neries-eu.org.

Hobiger, M., Bard, P.-Y., Cornou, C., and Le Bihan, N. (2009). Single station determination of Rayleigh wave ellipticity by using the random decrement technique (RayDec). *Geophys. Res. Lett.*, 36.

Maranò, S., Reller, C., Loeliger, H.-A., and Fäh, D. (2012). Seismic waves estimation and wavefield decomposition: Application to ambient vibrations. *Geophys. J. Int.*, 191:175–188.

Poggi, V. and Fäh, D. (2010). Estimating Rayleigh wave particle motion from three-component array analysis of ambient vibrations. *Geophys. J. Int.*, 180:251–267.

Wathelet, M., Jongmans, D., and Ohrnberger, M. (2004). Surface wave inversion using a direct search algorithm and its application to ambient vibration measurements. *Near Surface Geophysics*, 2:211–221.